

PROFILE SHAPE PARAMETERIZATION OF JET ELECTRON TEMPERATURE AND DENSITY PROFILES

Beatrix Schunke

JET Joint Undertaking, Abingdon, Oxon, OX14 3EA, UK

Kaya Imre and Kurt S. Riedel

New York University, 251 Mercer St., New York NY 10012-1185

Abstract

The temperature and density profiles of the Joint European Torus are parameterised using log-additive models in the control variables. Predictive error criteria are used to determine which terms in the log-linear model to include. The density and temperature profiles are normalised to their line averages (\bar{n} and \bar{T}). The normalised Ohmic density shape depends primarily on the parameter \bar{n}/B_t , where B_t is the toroidal magnetic field. Both the Low-mode (L-mode) and edge localized mode-free (ELM-free) high mode (H-mode) temperature profile shapes depend strongly on the type of heating power, with ion cyclotron resonant heating producing a more peaked profile than neutral beam injection. Given the heating type dependence, the L-mode temperature shape is nearly independent of the other control variables. The H-mode temperature shape broadens as the effective charge, Z_{eff} , increases. The line average L-mode temperature scales as $B_t^{.96}(\text{Power per particle})^{.385}$. The L-mode normalised density shape depends primarily on the ratio of line average density, \bar{n} , to the edge safety factor, q_{95} . As \bar{n}/q_{95} increases, the profile shape broadens. The current, I_p , is the most important control variable for the normalised H-mode density. As the current increases, the profile broadens and the gradient at the edge sharpens. Increasing the heating power, especially the ion cyclotron resonant heating, or decreasing the average density, peaks the H-mode density profile slightly.

PACS NUMBERS: 02, 52.55Fa, 52.55Pi, 52.65+z

1 INTRODUCTION

Scaling law-like expressions are needed to estimate the performance of the next generation of experimental fusion machines. While much effort has been spent on generating scaling laws for performance parameters, only the Ohmic temperature profile shapes have been parameterised in terms of the engineering variables^[1, 2, 3]. In this article, we report the results of the parameterisation of the Joint European Torus^[4] (JET) electron temperature profiles and density shapes for different confinement regimes. A preliminary version of this work was presented in Ref. [5]. These parameterised profiles summarise the typical temperature and density shapes as functions of engineering variables. We use the log additive models of Refs. [1, 2, 3] to represent the profiles in terms of the normalised toroidal flux radius, ρ , and the engineering control variables such as q_{95} , I_p , P_L , etc. The log-additive model is essentially a scaling expression for profile shapes:

$$T(\rho)/\bar{T} \quad \text{or} \quad n(\rho)/\bar{n} = \mu(\rho) I_p^{f_I(\rho)} \bar{n}^{f_n(\rho)} q_{95}^{f_q(\rho)} \dots \dots \quad (1)$$

There are at least six advantages of profile shape scalings. First, the shape scaling summarises the characteristic profile shapes over an operating period. Second, the fitted profiles serve as a benchmark against which new classes of discharges may be compared. Third, by fitting many discharges simultaneously, the signal to noise ratio is enhanced and we average over effects which are not reproducible from discharge to discharge. Fourth, these expressions can be used in transport, stability and heating codes as realistic temperature and density shapes. Fifth, in many cases, physics insight can be gained from examining the profile parameterisations. In particular, we are sometimes able to isolate similarity variables in the profile shape dependencies. Finally, in multi-machine databases, we can determine a size scaling and extrapolate the profile shape to new experiments such as the International Tokamak Experimental Reactor^[6] (ITER). Thereby, our methodology can predict the peaking factors and resulting fusion power production.

Our fitting methodology is described in Refs. [2, 3]. To choose which engineering variables to include in the fit, we minimise a model selection criterion. One result of this model selection procedure is that we use different variables to fit the Ohmic, low mode (L-mode) and high mode (H-mode) cases. We apply a similar sequential variable selection procedure in our linear regression analysis of the line average temperature scaling. To the best of our knowledge, sequential variable selection has never been used in global confinement analysis, and as a result, confinement scalings often include unnecessary and insignificant control variables. By using only the important control

variables, we imply that the other control variables barely influence the profile shape in our database. Thus, *we find the parameter directions where the profile shape is invariant.*

Our list of candidates for control variables includes engineering control variables such as the logarithms of the edge safety factor, q_{95} , the plasma current, I_p (in MA), the toroidal magnetic field, B_t (in Tesla), the average density, \bar{n}_e (in $10^{19}/m^3$), and the loss power, $P_L \equiv P_{aux} + P_{Ohm} - \dot{W}$ (in MW). We find that ion cyclotron resonant heating (ICRH) yields profile shapes different from the neutral beam injection (NBI) heating shapes. To measure this difference, we define a new variable, the heating fraction, H_{fr} , to be the ratio of ICRH to total auxiliary heating: $H_{fr} \equiv P_{ICRH}/[P_{NBI} + P_{ICRH}]$. We also examine for possible dependencies on the effective ion charge, Z_{eff} , and the plasma inductance, ℓ_i . We normalise the variables about their mean values in the data set. We do not consider the major and minor radii (R and a) and the plasma elongation, κ , because of their small variation in the data set. To determine the size dependence and examine intra-machine variability, a multi-machine database with an expanded parameter space is necessary. Work on a combined DIII-D-JET profile parameterisation has begun^[7, 8].

To measure the goodness of fit and determine which control variables influence the profile shape, we use the Predictive Absolute Residual (PAR) criterion as defined in the appendix. *The PAR criterion is our estimate of the expected absolute error in predicting the normalised profiles of new data taken under similar operating conditions.* The PAR criterion is the mean absolute residual error with a degree of freedom correction. The residual fit errors tend to be more uniform on an absolute scale than a logarithmic scale and appear to be nearly independent of the reported error bars. Thus we replace the Rice criterion (which assumes the errors are proportional to the reported error bars on a logarithmic scale) of Refs. [2, 3] with the PAR criterion which assumes the errors are uniform on an absolute scale. Using the sum of absolute residual errors instead of the sum of squared errors robustifies the criterion to outliers.

The choice of model selection criteria is somewhat arbitrary for real tokamak data because the data departs in unknown ways from the idealistic assumptions on which these criteria were based. We believe that the PAR criterion is robust and reasonably represents the size of the residual errors. Nevertheless, the exact choice of when to truncate the model and quit adding new control variables to the model is an art. As a rule, we quit adding terms when the PAR value only decreases slightly with the addition of a new term, and when several different control variables yield nearly the same PAR value. The PAR criterion and the Rice criterion usually agree on which control variables are important to keep in the fit. The Rice criterion sometimes wants to keep one more control variable in the model.

In addition to replacing the Rice model selection criterion with the PAR model

selection criterion, we make three other modifications of the fitting methodology in Refs. [2, 3]:

First, we normalise each temperature profile to its line average. (This is not an issue for the density profile since \bar{n} is a control variable.) We estimate the profile shape and the line average temperature separately. When we did not normalise the profiles, the errors in predicting the line average dominate the fit error. Normalising the profiles removes the uncertainty in the line average temperature, \bar{T} , and allows a more accurate parameterisation of the profile shape. To show that we are not losing information by fitting the normalised profiles and the line average temperature separately, we allow the shape model to depend on \bar{T} . We find that using \bar{T} as a predictor variable does not improve the profile shape parameterisation.

Second, we use only the measured data on the outboard flux radii and symmetrise the fit about $\rho = 0$. This change is based on the assessment of the relative reliability of the inboard and outboard measurement locations by the JET diagnostic team.

Third, we increase the spline penalty functional and thereby the smoothness of the fitted curves. Traditional data adaptive smoothness criteria attempt to minimize the predictive fit error in a particular function space. Surprisingly, minimising the predictive fit error results in curve estimates that tend to have false inflection points and spurious wiggles. These spurious wiggles can be eliminated with high probability if larger smoothing is used. We believe that achieving a correct estimate of the shape (correct number of inflection points) is more important than minimizing the model selection criterion with respect to the smoothness parameters. Thus we inflate the smoothness parameter by an amount which guarantees that asymptotically the shape of the estimate will be correct. This modest increase in the smoothness parameter has little impact on the final value of the residual fit error. For a more theoretical analysis of shape correct fits, we recommend Ref. [11].

Our predicted profiles are not “dimensionally correct” in the sense that they do not impose the Maxwell-Boltzmann constraint. Our predictions may be made dimensionless by adding a suitable exponent of the form $(R/R_{JET})^{f_R(\rho)}$, where $f_R(\rho)$ is determined by the linear constraint. (See Ref. [9] for the constraint procedure.) Our research^[10] indicates that the H-mode confinement violates the Maxwell-Boltzmann constraint, probably indicating the key role of radiation loss in many H-mode discharges.

In the fitting procedure, we do not explicitly require that the predicted profiles have a line integral equal to one. (We only normalise the data to correspond to profiles with a line integral equal to one.) Implementing the profile normalisation in the fitting procedure would require much programming effort and computational

cost. Not normalising the fitted profiles introduces a 2% error in the predicted line averages for the database. This error can be much more when our models are used to predict new profiles for parameters outside of the database range. To minimise these nonlinear errors, we recommend that our profile predictions be normalised to have a line integral to one.

2 DATA DESCRIPTION

We use databases of between 44 to 52 discharges. The discharges were taken from the experimental campaigns in 1989-92. The Ohmic and L-mode discharges are mostly limiter discharges with a beryllium-evaporated wall. Tables 2 and 3 summarise the L-mode and H-mode databases. The elongation, κ , varies by only 7.3% for H-mode and by only 9.9 % for L-mode. The typical value of the auxiliary heating differs considerably in the two cases. For the (H-mode database, the mean is 8.0 MW while it is only 4.8 MW for the L-mode database. This difference is due to the H-mode power threshold.

The H-mode discharges are typical H-mode discharges from 1989-92, and therefore are predominately edge localized mode-free (ELM-free). Our method assumes that the plasma profiles are time stationary. A significant number of H-mode profiles are still evolving to a limited extent, and thus our H-mode fit results may be influenced by the ongoing temporal evolution of the profiles.

The flux radius is normalised such that the toroidal flux through a given radius, ρ , is equal to ρ^2 times the total flux. In our previous articles^[2, 3], we used the normalised poloidal flux radius, $\bar{\psi}$, instead of the normalised toroidal flux radius. For the line average, we use $\bar{n} \equiv \int_0^1 n(\rho)d\rho$ instead of the more common definition of $\bar{n} \equiv \int n(R)dR / \int dR$. For each profile, we calculate the line average electron density from the Light Detection And Ranging (LIDAR) diagnostic measurements instead of using the interferometry measurement. We use the line averages of the temperature and density instead of the volume averages, however this choice is done for convenience only. We expect similar results to hold for the volume averages.

The electron temperature and density profiles are measured by the JET LIDAR Thomson scattering diagnostic^[12]. Each profile is measured at approximately 50 radial locations along the plasma mid-plane. As discussed in Ref. [3], neither the profile measurements nor the accuracy of the measurements are symmetric with respect to ρ . The outboard side measurements are more accurate than the inboard side. Thus, we use only the outboard side measurements, and we require that the fitted func-

tions be symmetric in ρ . We find that 10 internal knots are adequate to describe the shape. The LIDAR measurements usually have higher edge temperatures than the ECE measurements on JET. Our temperature profile parameterisation represents the LIDAR measurements.

Our present results supercede our earlier results in Refs. [2, 3].

3 OHMIC PROFILE FIT

3.1 Ohmic Density

The Ohmic database is described in Ref. 3. Table 1 summarises the variation of the control variables. We normalise the density by its line average, \bar{n} : $n(\rho)/\bar{n}$. Normalisation of the profiles greatly reduces the fit error. We define $y_{i,j} \equiv \ln[n_{i,j}/\bar{n}_i]$, where $n_{i,j}$ is the measured electron density of the i th profile at the j th radial location.

We begin by considering all possible two-term fits to the data of the form: $y_{i,j} = f_0(\rho_j) + f_1(\rho_j) \ln[u_i]$, where $f_0(\rho_j)$ and $f_1(\rho_j)$ are spline functions and u_i is the value of the control variable, u for the i th profile. The first column of Table 4 is a list of control variables, where the logarithmic transformation is implicitly assumed. The second column is the PAR goodness of fit when a single control variable is used in the fit. Of the standard control variables (not including \bar{n}/B_t), the most effective in reducing the PAR statistic is the average density, \bar{n} . The third column gives the PAR goodness of fit criterion when we use two control variables in the fit, the first of which is \bar{n} . Using both \bar{n} and B_t reduces the PAR statistic from .0612 to .0567.

The fourth column shows that the goodness of fit is not improved by fitting the data with three control variables (\bar{n} , B_t , and one other variable). Figure ?? plots $\mu(\rho) = \exp(f_0(\rho))$, $f_n(\rho)$ and $f_B(\rho)$. Here $\mu(\rho)$ is our predicted profile when \bar{n} and B_t are chosen at their geometric means. Thus $\mu(\rho)$ corresponds to the canonical normalised Ohmic density profile. At $\rho = .75$, the gradient of $\mu(\rho)$ becomes steeper. Since $f_n(\rho)$ is negative in the interior and positive beyond $\rho = .4$, our predicted profile broadens as the average density increases.

The most striking result of Figure ?? is that $f_n(\rho) \approx -f_B(\rho)$. To very good approximation, the shape depends on \bar{n} and B_t only through the ratio, \bar{n}/B_t . Since the major radius is fixed in JET, \bar{n}/B_t is a Murakami-like variable. The Murakami parameter is associated with increased radiation near the density limit. This offers some potential insight into the physics of the Ohmic density profile variation being related to radiated energy loss.

The slight difference between the two curves ($f_n(\rho)$ and $-f_B(\rho)$) near $\rho = 1.0$

indicates that increasing both quantities equally will lead to a slight broadening of the edge. We do not believe that this difference is significant. To show this, we refit the model using only the ratio, \bar{n}/B_t , as a control variable. The resulting PAR value, .0561, is lower than using both \bar{n} and B_t separately. This shows that using two free functions is not worth the cost of the extra degrees of freedom.

The final column of Table 4 examines the fit when two control variables are used, one of which is \bar{n}/B_t . The goodness of fit is not improved significantly by adding a third control variable. Therefore, we adopt the one control variable model using only \bar{n}/B_t :

$$n(\rho) = \bar{n} \mu(\rho) \left(\frac{\bar{n}}{B_t} \right)^{f_{n/B}(\rho)}, \quad (2)$$

where we assume that $\frac{\bar{n}}{B_t}$ has been normalised to its mean value. Figure ?? plots our predictions versus the data for the profile with the largest value (1.28) of \bar{n}/B_t and for the profile with the smallest value (0.44). At $\bar{n}/B_t = 1.28$, our predicted profile is just beginning to be hollow. The fitted profiles do not attempt to track the slight flattenings in the data that are due to either random measurement noise or possibly nonreproducible magnetic islands. Instead, the fitted profiles model the diffusive part of the profiles and average over the local flat spots.

3.2 Ohmic Temperature

Our previous Ohmic temperature fit is described in detail in Ref. 3. To a reasonable degree of accuracy, the JET Ohmic electron temperature profile can be fit with the “profile resilient” form:

$$T(\rho) = \mu(\rho) q_{95}^{f_q(\rho)} \quad (3)$$

A more accurate fit to the data is adding a magnetic field dependence:

$$T(\rho) = \mu(\rho) q_{95}^{f_q(\rho)} B_t^{f_B(\rho)}, \quad (4)$$

which reduces the PAR value from .0812 to .0755. The final column of Table 5 shows that little improvement in the fit occurs when a third variable is added. We believe that the dependence on plasma elongation is not real due to the small amount of κ variation in the data set. Instead, we believe that the observed κ dependence is due to hidden variables (differences in machine operation) which correlate with κ variation in this data set. Thus we accept the two variable model of Eq. (4).

The final row of Table 5 uses the line average temperature as a regression variable. Since the fit barely improves when \bar{T} is used, this demonstrates that the temperature shape and magnitude are uncorrelated.

Figure ?? plots $\mu(\rho) = \exp(f_0(\rho))$, $f_q(\rho)$ and $f_B(\rho)$. Here $\mu(\rho)$ is our predicted profile when q_{95} and B_t are chosen at their geometric means. The canonical normalised Ohmic temperature profile, $\mu(\rho)$, is bell-shaped. Increasing I_p and q_{95} corresponds to changing the shape according to $f_q(\rho)$. Higher q_{95} and I_p result in a more peaked profile. From our previous study^[3], we believe that changing q_{95} with fixed I_p and fixed B_t should change the profiles less. This $\hat{q} \equiv q_{95}I_p/B_t$ effect is not in our present model.

When q_{95} is increased by increasing both B_t , the profile shape change corresponds for $f_q(\rho) + f_B(\rho)$. Thus changes in B_t cause little effect near the center, but very sharp changes in the edge gradient. Figure ?? plots our predictions versus the data for the profile with the largest value (12.6) of q_{95} and for the profile with the smallest q_{95} (2.88) in the data set. The local flat spots are not described by our model when they are not reproducible. Instead, the fitted profiles average over the local flattening and correspond to the net diffusive profile.

In Eq. (4), the \bar{T} dependence is unknown. We fit the line average temperature with a power law in the control variables using a log-linear regression. We find that a three-parameter model using I_p , \bar{n} and B_t fits the line average temperature:

$$\bar{T} = .505 I_p^{.64 \pm .04} B_t^{.54 \pm .09} (\bar{n})^{-.31 \pm .06} . \quad (5)$$

The degree of freedom corrected root mean square error (RMSE) is 11.5 %. The most surprising part of the \bar{T} regression is that $\bar{T} \sim (\bar{n})^{-.31}$ instead of the often assumed scaling of $\bar{T} \sim (\bar{n})^{-1.0}$. In Ohmic plasmas, the heating rate is coupled to the line average density so it is not surprising that $\bar{T}\bar{n} \neq \text{constant}$. Our L-mode and H-mode results confirm that the line average temperature has a relatively weak density dependence in JET. In Ref. [1], Ohmic results for the axisymmetric divertor experiment^[13] (ASDEX) are given: $\langle T_e^{ASDEX} \rangle \sim I_p^{.95} B_t^{.04} (\bar{n})^{-.56}$, where we have averaged the two ASDEX scalings. Thus JET has a weaker density dependence, a different q_{95} dependence and a stronger magnetic field dependence. All of these differences in the \bar{T} scaling are consistent with the differences in confinement scalings^[9]. One of the important results of Ref. [1] is that the plasma energy shows no roll-over regime at high density. The flattening in confinement time in ASDEX correlates with an increase in the loop voltage, allowing the plasma energy, W , to scale similarly in both regimes. Similarly, we suspect that the \bar{T} will change only slightly in the roll-over regime.

4 L-MODE PROFILES

4.1 L-mode Density

In analyzing auxiliary heated discharges, we add two more control variables: the loss power, $P_L \equiv P_{aux} + P_{Ohm} - \dot{W}$ (in MW), and the heating fraction, $H_{fr} \equiv P_{ICRH}/[P_{NBI} + P_{ICRH}]$. We find that ion cyclotron resonant heating (ICRH) produces different profile shapes than neutral beam injection (NBI) heating produces. We believe that this difference is due to changes in the power deposition profile and changes in the fast particle population. In the future, we hope to examine more physical parameterizations of the heating effectiveness^[14]. For this study, we use the heating fraction because it is easily evaluated. In the L-mode data set, 28 of the discharges are predominately (more than 50 %) ICRH-heated and 24 are predominately NBI-heated.

Table 6 presents the goodness of fit as the number and choice of control variables is varied. The most important control variable is the line average density, \bar{n} . The first column of Table 6 shows that using only \bar{n} yields a PAR of value of .0633. If \bar{n} is replaced by \bar{n}/B_t , the misfit increases to a PAR of .0641. As seen from Fig. ??, $f_n(\rho)$ is shaped like a convex parabola. This implies that as the average density increases, the profile broadens. It is reassuring that our statistical model agrees with this common experimental observation.

The second most important variable (given that \bar{n} is used) is the edge safety factor, q_{95} . The two control variable model has a PAR value of 0.0619. The $f_q(\rho)$ curve in Fig. ?? is shaped like a concave parabola. Note that $f_q(\rho) \approx -f_n(\rho)$. Thus increasing both the edge q and the density by the same relative amount should result in little change in the profile shape. The approximate relation, $f_q(\rho) \approx -f_n(\rho)$, tempts us to replace the two-parameter fit with a new model involving only the ratio, \bar{n}/q_{95} .

The third column of Table 6 shows the goodness of fit for three control variable models given \bar{n} and q_{95} . The addition of the heating fraction, H_{fr} reduces the PAR value to .0606. From Fig. ??, increasing the fraction of ion cyclotron heating tends to broaden the density profile. This may indicate that ICRH tends to increase the inward pinch of particles. Alternative explanations are discussed in the L-mode temperature section.

Column 4 of Table 6 shows that the adding additional variables does not appreciably improve the residual error. Thus, we select the L-mode model:

$$n(\rho) = \bar{n} \mu(\rho) (\bar{n})^{f_n(\rho)} q_{95}^{f_q(\rho)} \exp(f_H(\rho)H_{fr}) . \quad (6)$$

Figure ?? plots our predictions versus the data for the profile with the largest value ($5.63 \times 10^{19}/m^3$) of \bar{n} and for the profile with the smallest value ($0.78 \times 10^{19}/m^3$). Since we fit 52 profiles simultaneously, the predicted curves follow the reproducible part of the profile and neglect the local flattenings which vary from discharge to discharge.

4.2 L-mode temperature

The model selection criterion (PAR) shows that the heating fraction, $H_{fr} \equiv P_{ICRH}/[P_{NBI} + P_{ICRH}]$ is the only control variable that is necessary to parameterise the L-mode temperature profile shape. The first column of Table 7 shows that the PAR value is much smaller when H_{fr} is used than with any other single control variable. The second column shows that the goodness of fit does not improve if a second control variable is added to the model. Using three control variables, H_{fr} , P_L and I_p , reduces the PAR value insignificantly from .0869 to .0868. Our judgement is that this reduction in fit error is insufficient to justify adding two additional control variables to the model. Therefore, we recommend the one-parameter model:

$$T(\rho) = \bar{T} \mu(\rho) \exp(f_H(\rho)H_{fr}) . \quad (7)$$

Figure ?? shows $\mu(\rho)$ and $f_H(\rho)$. Here, $\mu(\rho)$ corresponds to the database mean of the normalised temperature profile. Thus, the canonical profile $\mu(\rho)$ has a bell shape. The heating factor function, $f_H(\rho)$, shows that increasing the percentage of ICRH power to NBI power results in increasingly peaked profile shapes. This shape dependence could be due to the different power deposition profiles of ICRH and NBI. In Ref. [14], it is shown that the temperature profile shape varies as the resonance layer for ICRH is shifted outward. Since the NBI power deposition profile is broader than the typical ICRH deposition profile, our shape parameterisation is consistent with the results in Ref. [14]. Another factor in the heating type dependence is the reduction of sawtooth activity with ICRH. The underlying physical mechanism is that fast particles stabilise the sawtooth at least partially, thereby reducing the sawtooth frequency.

In our previous analysis (using the poloidal flux, $\bar{\psi}$, instead of the toroidal flux, ρ), the toroidal magnetic field influenced the profile shape. Using the normalised toroidal flux radius as the spatial coordinate makes the profile shape nearly independent of the magnetic field magnitude. Note that the mapping $\bar{\psi}$ to ρ depends on the safety factor, $q(\rho)$.

In Eq. (7), the \bar{T} dependence is unknown. We fit the line average temperature with a power law in the control variables using a log-linear regression. Since not all

control variables are necessary to fit \bar{T} , we again use a sequential selection procedure to choose which variables are important to include in the regression. We find that a three parameter model using P_L , \bar{n} and B_t fits the line average temperature:

$$\bar{T} = .705 B_t^{.97 \pm .16} (\bar{n})^{-.38 \pm .07} P_L^{.36 \pm .05} . \quad (8)$$

The corrected RMSE is 20.0 %, indicating that the power law model may not be appropriate for the line average temperature. Equation (8) can be interpreted as *Temperature / $B_t \sim (\text{Power per particle})^4$, which is a gyro-Bohm scaling*. Thus we see that the electron temperature is gyro-Bohm while the global confinement time is Bohm-like. The main surprise of our \bar{T} fit is that there is no dependence on the plasma current in our fitted expression. Note that I_p varies by a factor of four; thus the lack of a current dependence is highly significant. Most tokamaks tend to observe a dependence such as $I_p^{.85} B_t^2$ for the L-mode confinement time. For JET, the L-mode confinement^[9] tends to scale as $\tau_E \sim I_p^9 B_t^5$, which shows more of a B_t dependence. Equation (8) indicates that the improvement in L-mode confinement time with increasing B_{pol}/B_t is not due to improved confinement of bulk electrons. Thus the I_p dependence of the τ_E scaling is associated with improved confinement of ions or fast particles or possibly due to a reduction in Z_{eff} and the corresponding increase in ion density.

Figure ?? plots our predictions versus the data for a profile with only NBI heating and for a profile with only ICRH. For this particular ICRH-only profile, our prediction is less peaked than the measured profile. Nevertheless, the prediction is easily within 2σ .

5 H-MODE PROFILES

Our H-mode data set consists predominately of ELM-free discharges, that were typical of H-mode operation in the period 1989-92. Many of these discharges are evolving to a greater or lesser extent. This nonstationary behavior makes our H-mode profile parameterization somewhat less reliable than our corresponding Ohmic and L-mode parameterisations. In the L-mode data set, 28 of the discharges are predominately (more than 50 %) ICRH-heated and 20 are predominately NBI-heated.

5.1 H-mode Density

Figure ?? displays the predicted profile at geometric mean of the normalised density profiles. The canonical ELM-free H-mode profile is much flatter than the correspond-

ing canonical L-mode profile (Fig. ??). Even at $\rho = 1.0$, the local density is more than 60 % of the central density.

The total current is the most important control variable in reducing the model selection criteria. Increasing the total current, I_p , flattens the normalised density profile. As a result, the edge gradient steepens. At the largest values of I_p , the density profile is often hollow. The second most important control variable is the loss power, P_L . Figure ?? shows that increasing heating power broadens the profile in the central region. In contrast to the current dependence, increasing the input power does not lead to large changes in the edge gradient. This effect is seen in Figure ??, since $f_P(\rho)$ is smaller than $f_I(\rho)$ near $\rho = 1$. Table 8 presents the model selection criteria. The PAR statistic decreases from .0619 to .0597 when P_L is added to the model. From the third column of Table 8, we see that adding either the line average density or the heating fraction reduces the PAR statistic to .0584. The fourth column shows that the PAR value reduces to .0563 when both the line average density and the heating fraction are added.

Figure ?? shows that increasing the average density broadens the density profile but does not effect the edge gradient. Increasing the heating fraction of ICRH results in somewhat more peaked H-mode density profiles. The opposite heating fraction dependence is observed in L-mode, where ICRH broadens the density profile. Our final H-mode density model is

$$n_e(\rho) = \bar{n} \mu(\rho) I_p^{f_I(\rho)} P_L^{f_P(\rho)} (\bar{n})^{f_n(\rho)} \exp(f_H(\rho)H_{fr}) . \quad (9)$$

Figure ?? plots our predictions versus the data for both the profile with the largest value (3.18) of I_p and the profile with the smallest value (2.07) in the data set. The fit quality is good for the $I_p = 3.18$ case, while the $I_p = 2.07$ case is more peaked than our prediction. This small misfit occurs because other low current discharges in our database are much less peaked than # 27215. The predicted profiles show a local flattening near $\rho = 0.9$. This feature is present in a large percentage of the data set and therefore, our model tracks this reproducible flattening.

5.2 H-mode Temperature

The database mean of the normalised temperature is seen in Fig. ?. The ELM-free H-mode canonical profile shape is broader than the corresponding mean profile for L-mode. Outside of $\rho = 0.2$, the normalised temperature gradient decreases more slowly than the L-mode gradient.

The most important control variable in predicting the H-mode temperature shape is the heating fraction. As in L-mode, ICRH heating creates much more peaked

profiles than does the equivalent heating with NBI. Comparing the response functions for $f_H(\rho)$ for H-Mode (Fig. ??), and for L-mode (Fig. ??) shows that the two curves have similar shapes, but that the H-mode function is less peaked in the H-mode case. This indicates that the L-mode profile shape is more sensitive to the type of heating than is the ELM-free H-mode

Table 9 displays the model selection criteria as we increase the number of control variables in the model. When only the heating fraction is used, the PAR statistic is .0650. If the effective charge is added, the PAR value is .0632, while using the line average density instead of Z_{eff} yields a worse value of .0640. We believe that this difference is large enough that we choose Z_{eff} as the second control variable. We should caution that the errors in Z_{eff} are appreciably larger than in the other control variables. Also, Z_{eff} is a spatially varying quantity and we are parameterizing the impurity distribution using one chordal measurement. A final caution is that $f_Z(\rho)$ is largest at the plasma edge, corresponding to the edge temperature increasing with increasing Z_{eff} . Since a higher edge temperature will produce impurities, our results could be interpreted as saying that broader temperature profiles create more impurities. Our fit only shows that higher Z_{eff} correlates with broader profiles, and we cannot comment on the causality issue. Even if the edge temperature is creating the Z_{eff} , our fit shows how the entire temperature profile shape response to the resulting impurity influx.

The last column of Table 9 shows that the fit does not improve when a third parameter is added. Thus the sequential selection procedure suggests the two control variable model:

$$T(\rho)/\bar{T} = \mu_0(\rho)Z_{eff}^{f_Z(\rho)} \exp(f_H(\rho)H_{fr}) . \quad (10)$$

Since $f_Z(\rho) \approx -f_H(\rho)$, our profile shape depends almost exclusively on $H_{rf} - \ln[Z_{eff}]$. Figure ?? plots our predictions versus the data for the NBI heating-only profile with the smallest Z_{eff} concentration (1.07) and for the ICRH-only profile with the largest Z_{eff} concentration (5.43). The control variable, $H_{rf} - \ln[Z_{eff}]$ is -.068 for the NBI discharge and -.692 for the ICRH discharge; thus our model predicts that this particular dirty ICRH discharge should be broader than the clean NBI discharge. Our prediction is in clear agreement with the data, indicating that the Z_{eff} effect can negate the difference in heat type.

The line average temperature has been regressed using a sequential selection procedure. Our best fit yields

$$\bar{T} = .649I_p^{1.22 \pm .17} P_L^{.29 \pm .08} (\bar{n})^{-.23 \pm .13} \exp((.24 \pm .08)H_{fr}) . \quad (11)$$

The corrected RMSE is 19.8 %, again indicating that the line average temperature

may not follow a power law scaling. Similarly to L-mode, the line average temperature depends on \bar{n} and P_L only through the ratio of P_L/\bar{n} (to good approximation), corresponding to the power per particle. The line average temperature has a weak density dependence $(\bar{n})^{-.246}$. If we assume that the total plasma energy scales proportionally to $\bar{n}_e \bar{T}_e$, then Eq. (11) implies that the plasma energy would scale as $\bar{n}^{.75}$. This result is consistent with a gyro-Bohm scaling, but differs from the commonly observed confinement dependence of $\tau_E \sim \bar{n}^{.15}$. Part of this discrepancy may be explained because fast particle confinement degrades with increasing density.

The power scaling in Eq. (11) is consistent with a confinement scaling of $\tau_E \sim P_L^{-.7}$, in agreement with most scaling expressions. The line average temperature has an even stronger current dependence than the corresponding confinement time has (typically^[15] $\tau_E \sim I_p^{.85}$ to $I_p^{1.0}$.) We note that q_{95} and I_p vary roughly half as much in the H-mode database as in the L-mode database. As such, the uncertainty in the scalings with q_{95} and I_p is larger in H-mode. Nevertheless, the I_p variation is sufficiently large to show that the H-mode density profile shape has a highly significant I_p dependence.

6 DISCUSSION

Our parameterizations of the JET normalised temperature profiles fit the LIDAR measurements with a mean predictive error of .075 for Ohmic, .063 for H-mode and .087 for L-mode. The corresponding density fits have PAR values of .056 for Ohmic, .056 for H-mode and .061 for L-mode. Thus our fits accurately describe the profiles in our database, and they may be used in the modeling of these discharges as a proxy for the real data.

The model selection criteria determine which control variables are most important. Table 10 summarises which variables modify the profile significantly in each regime. In both L-mode and H-mode, the heating type dominates the profile shape due to either power deposition effects or sawtooth stabilization. The Ohmic density profile depends only on the Murakami parameter, and thus the profile broadening appears to be related to radiation effects. The L-mode density profiles depend on the line average density with broader profiles corresponding to higher densities, while the H-mode density depends primarily on the plasma current. If a control variable is not used in our parameterization, it means that the omitted variable was not necessary to include in the modeling.

Physics trends are often discernible from the profile fit. One clear line of research is to explain the observed parametric dependencies as summarised in Table 10. The

most tantalizing physics results are the shape dependencies on heating type and the \bar{n}/B_t dependence of the Ohmic density.

We caution that our results are based on a subset of the JET discharges. Our existing data contains a variety of different discharges which are representative of typical JET operating regimes. We fully expect that our findings are representative of the usually observed JET profile dependencies. Our H-mode data set is identical to the data set which we later used in the initial DIII-D-JET H-mode comparison in collaboration with Dave Schissel^[7]. In this article, we include slightly different sets of control variables than in the combined fit. The parameterization given here is optimised to give an accurate fit to the JET data set alone. In Ref. [7], the control variables and resulting parameterization were optimised to fit both machines simultaneously.

We stress that our log-additive profile fits are only an approximation of reality. Our philosophy is “All models are wrong; some are useful.” We believe that our power law expressions fit the data well and can be used as summary of existing JET results and as a benchmark for new results. These expressions summarise the observed profile shape as a function of the control variables.

Our profile parameterisations may be used directly in analysis codes. By fitting many discharges simultaneously, we reduce the discharge-to-discharge variation at the cost of making systematic model errors. These model errors are typically small in the parameter region where the data is taken, but can be large when the parameterization is extrapolated into new regimes. Since our fits can be evaluated in real time, they can be used in plasma control systems. In the near future, they will be evaluated on-line as part of the JET LIDAR diagnostic. Thus, one can quickly compare a particular discharge temperature and density shapes with “standard” JET results.

ACKNOWLEDGMENTS

G. Cordey’s support and encouragement are gratefully acknowledged. We thank C. Gowers for his many helpful suggestions. The final revision of this paper has benefited significantly from our new collaboration with Dave Schissel. We thank the referees for their useful comments.

KI’s work was supported by the U.S. Department of Energy Grants No.DE-FG02-92ER54157 and 86ER-53223. KSR’s work was supported by the U.S. Department of Energy Grants DE-FG02-86ER-53223 and 91ER54131.

APPENDIX: PREDICTIVE ERROR ESTIMATION

In the present article, we use the predictive absolute residual (PAR) criterion to select which terms to measure the goodness of fit and determine which control variables influence the profile shape:

$$\mathbf{PAR} = \sum_{i,j} \frac{|T_i(\rho_j) - \hat{T}(\rho_j, \mathbf{u}_i)|}{N - 2 \times \# \text{ of free parameters}} , \quad (12)$$

where $T_i(\rho_j)$ is the measurement of the normalized temperature of the i th profile at the j th measurement location, and \hat{T} is the corresponding fitted value of the normalised temperature (or normalised density) as a function of the vector of control variables, \mathbf{u} . In the denominator of Eq. (12), N is the total number of measurements. Since we are using smoothing splines, the number of free parameters decreases as the smoothness penalty increases. In the appendix of Ref. [3], our definition of the number of free parameters in a spline fit is given. The factor of two accounts for the increased difficulty in predicting new data instead of fitting the existing data. As the number of free parameters increases, the denominator tends to make the PAR value increase. This effect tends to counterbalance the improvement in the residual error from adding more free parameters.

The PAR statistic is simply the least absolute value analog of the Rice criterion, C_R , which we used in our previous work^[2, 3]:

$$C_R \equiv \frac{1}{N - 2 \times \# \text{ of free parameters}} \sum_{i,j} \frac{|\ln[T]_i(\rho_j) - \ln[\widehat{T}](\rho_j, \mathbf{u}_i)|^2}{\sigma_{i,j}^2} , \quad (13)$$

where $\sigma_{i,j}^2$ is the variance of the measurement $\ln[T]$ for the i th profile and j th measurement location. In the appendix of Ref. [3], we give a derivation the Rice criterion.

The PAR criterion is our estimate of the expected absolute error in predicting the normalised profiles of new data taken under similar operating conditions. In theory, $(N - 2p)PAR * \sigma^2$ has approximately a χ^2 distribution with $(N - 2p)$ degrees of freedom where p is the effective number of degrees of freedom in the model. Given the large amount of data, $N - 2p \sim 2000$, and the significant departures of the data from the simple assumptions of the statistical model, we do not trust the PAR statistic to determine when to truncate the model. Instead, we stop adding terms to the model when several different control variables yield a similar reduction in the PAR criterion.

The PAR statistics sums the *absolute values* of the fit errors while the Rice criterion sums the *squares* of the fit errors on the logarithmic scale normalized to the standard deviation of the measurement error. Standardizing the residual errors to the measurement errors is optimal when the fit error is proportional to the measurement

error. In practice, our fit errors are only weakly correlated with the measurement error size. A reasonable hypothesis is that the systematic error portion of the fit error is uniform and uncorrelated with the measurement error size.

By using the absolute value, the PAR statistic is more robust in the sense that it is less sensitive to a small number of points which fit poorly. As is standard in robust statistics, we use the degree of freedom correction for Gaussian statistics, but replace the sum of squares estimate of the residual variance with a robustified analog. The PAR statistic corresponds to the visual quality of fit while the Rice criterion tends to measure the fit error near the plasma edge where the fit error is the largest on the relative scale. When one or two profiles have large residual fit errors, the Rice criterion will depend sensitively on the residual errors of these profiles due to its quadratic weighting. In contrast, the PAR statistic does not emphasise the most poorly fitting profiles due to its linear weighting, and therefore is more robust. The Rice criterion can be evaluated much more rapidly, and we use it for optimizing the smoothing parameters. We use PAR to determine which covariants to include in the model.

In our earlier analyses^[2, 3], we minimise Eq. (13) with respect to the smoothing parameters. This yields a smoothing parameter, λ_R , which is nearly optimal with regard to predictive mean square error. However, the resulting estimated curves often have spurious wiggles which we do not believe are actually present. To remove these wiggles, we increase the smoothing parameter by a factor of $\ln(N)$. The logarithmic factor suppresses artificial wiggles with asymptotic probability one^[11].

An older (obsolete) statistic is χ^2 , which replaces the denominator of $(N - 2 \times \#$ of free parameters) with $(N - \#$ of free parameters), and thereby corresponds to the mean square error per degree of freedom. The χ^2 statistic is useful in optimizing the fit to existing data, while the Rice criterion minimises the predictive error for new data. The factor of two in the denominator of PAR and C_R accounts for the greater difficulty in predicting new data than in fitting existing data. This factor of two in the denominator of C_R results in smoother models and fewer variables in the model.

References

- [1] MCCARTHY, P. J., RIEDEL, K. S., KARDAUN, O. J., Nuclear Fusion **31**, 1595 (1991).
- [2] RIEDEL, K. S., and IMRE, K., Comm. in Statistics **22** (1993) 1795.
- [3] IMRE, K., RIEDEL, K. S. and SCHUNKE, B., Physics of Plasmas **2** (1995) 1614.
- [4] REBUT, P. H., and KEEN, B. E., Fusion Technology **11** (1987) 13.
- [5] SCHUNKE, B., IMRE, K. and RIEDEL, K. S., in Controlled Fusion and Plasma Physics (Proc. 21st European Conf. Montpellier, 1994) Vol. 18B, Part II, Physical Society Plasma Physics Conference Proceedings, European Physical Society, Geneva (1994) 668.
- [6] POST, D. E., BORRASS, K., CALLEN, J. D., et al., *I.T.E.R. Physics Basis*. International Atomic Energy Agency Publishing, Vienna (1991).
- [7] SCHISSEL, D.P., SCHUNKE, B., IMRE, K. and RIEDEL, K. S., in Controlled Fusion and Plasma Physics (Proc. 22st European Conf. Bournemouth, 1995) Vol. 19C, Part II, Physical Society Plasma Physics Conference Proceedings, European Physical Society, Geneva (1995) 65.
- [8] IMRE, K. RIEDEL, K. S., SCHISSEL, D., and SCHUNKE, B., “H-mode profile parameterization for extrapolation & control” Accepted for publication in *Plasma Physics and Controlled Fusion*.
- [9] RIEDEL, K. S., Nuclear Fusion **31** (1991) 927.
- [10] RIEDEL, K. S., Nuclear Fusion **32** (1992) 1270.
- [11] RIEDEL, K. S. “Two Stage Estimation of Piecewise Convex Functions.” Proceedings of the third ICIAM, ZAMM, (1996).
- [12] SALZMANN, H. BUNDGAARD, J., GADD, A., et al., Rev. Sci. Instrum. **59**, (1988) 1451.
- [13] KEILHACKER, M., and the ASDEX team, Nuclear Fusion **25** (1985) 1045.
- [14] CALLEN, J. D., CHRISTIANSEN, J. P., CORDEY, J. G., et al., Nuclear Fusion **27** (1987) 1857.

- [15] YUSHMANOV, P., TAKIZUKA, T., RIEDEL, K. S., et al., Nuclear Fusion **30** 1999 (1990) 1999.

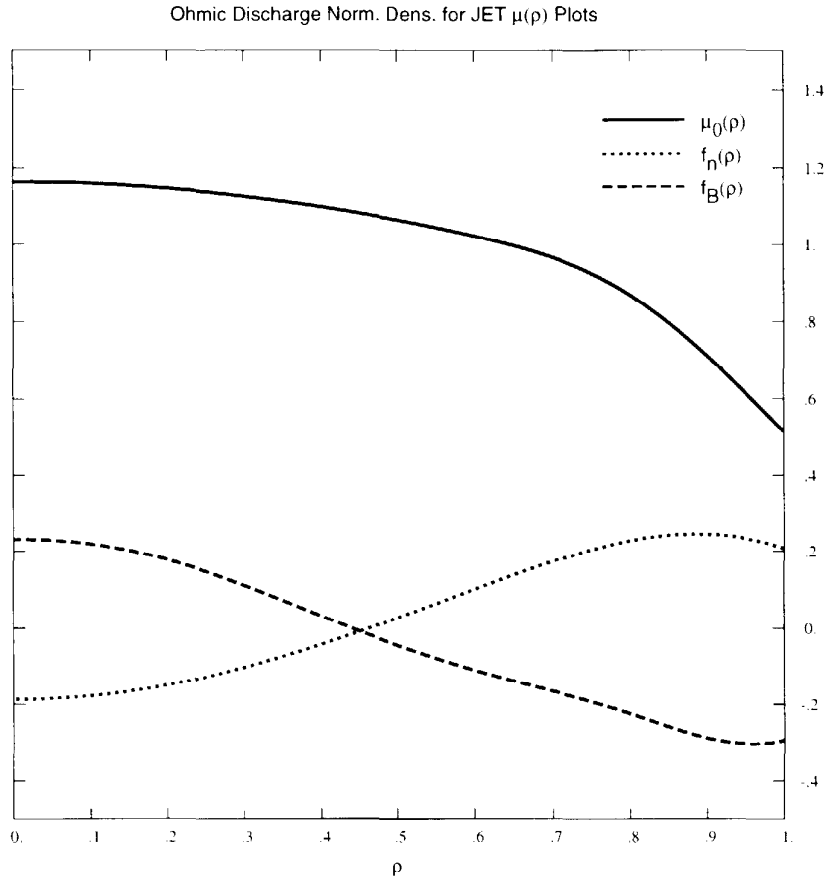


Figure 1

FIG.1. Fit functions for the normalised Ohmic density profiles. Here $\mu_0(\rho)$ gives the fitted profile at $\bar{n}/B_t = 0.765$. The profile becomes hollow with increasing \bar{n}/B_t .

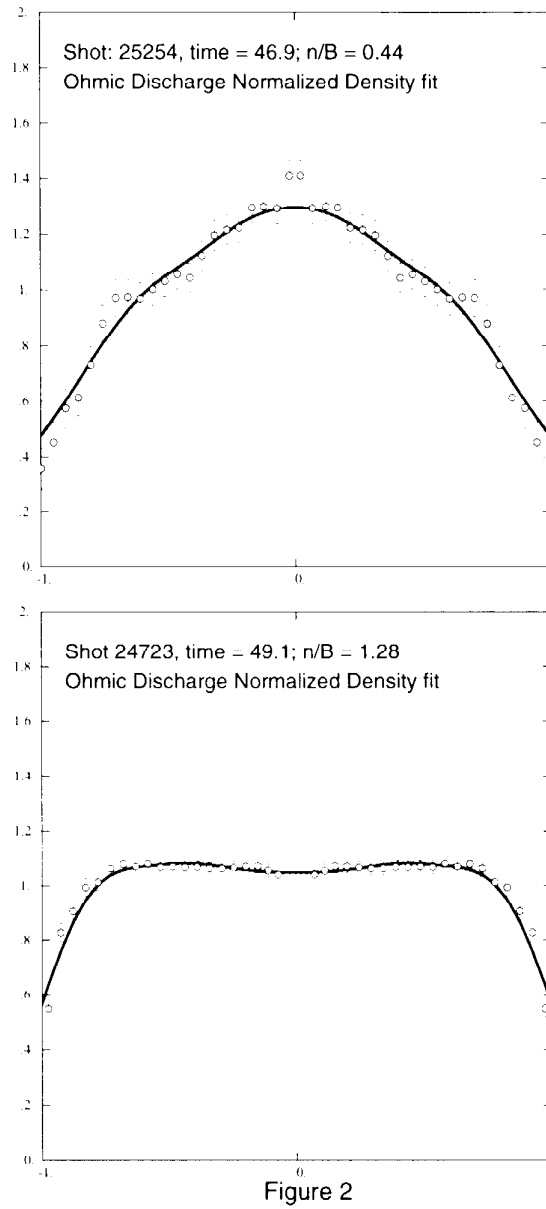


FIG.2. Normalised data versus the predicted Ohmic density profile. The broader curve (JET discharge #24723 at time = 49.1 sec) has the largest value of \bar{n}/B_r (1.28) in the data set. The narrower curve (JET discharge #25254 at time = 46.9 sec) has the smallest value of \bar{n}/B_r .

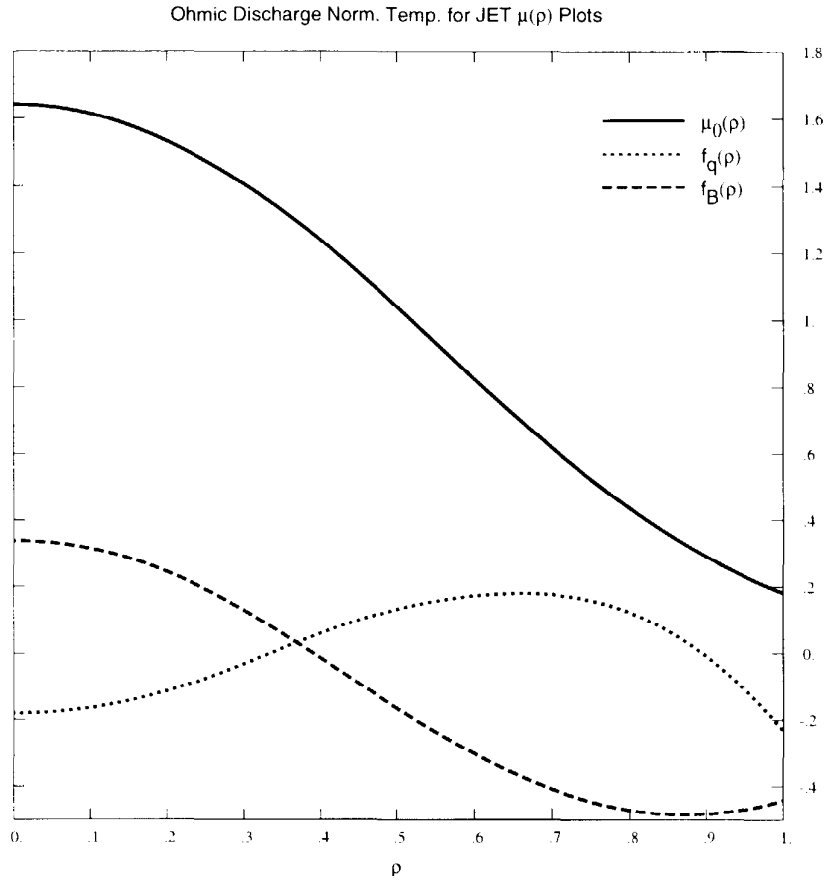


Figure 3

FIG.3. Fit functions for the normalised Ohmic temperature profiles. Here $\mu(\rho)$ gives the fitted profile at $q_{95} = 4.968$, $B_t = 2.72$ T. The profile becomes peaked with increasing q_{95} or decreasing I_p

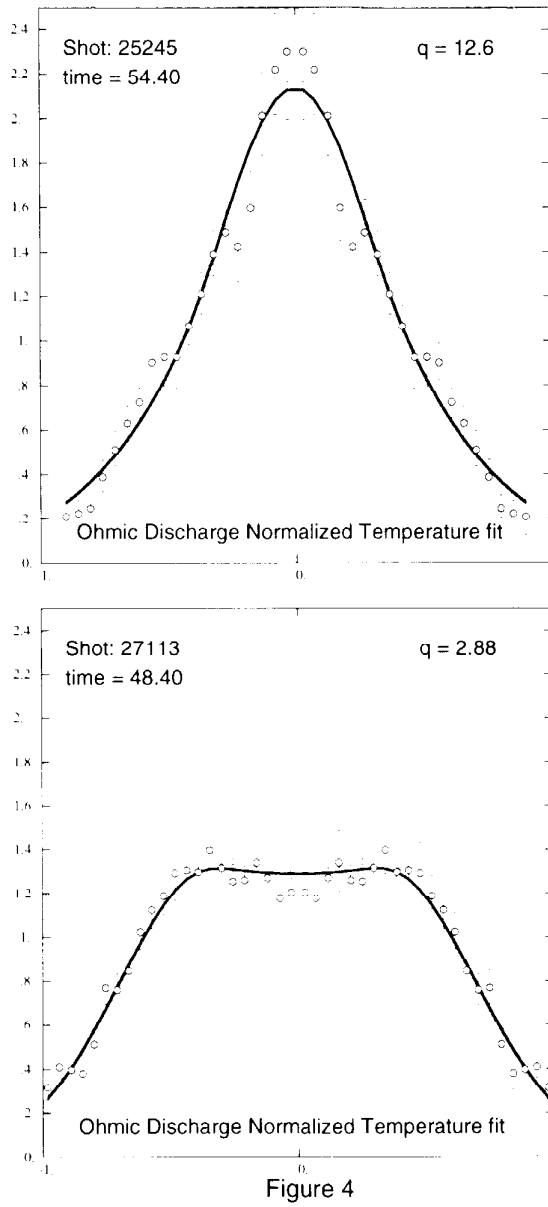


Figure 4

FIG.4. Normalised data versus the predicted Ohmic temperature profile. The broader curve (JET discharge #27113 at time = 48.4 sec) has the largest value of q_{95} (2.88) in the data set. The narrower curve (JET discharge #25245 at time = 54.4 sec) has the smallest value of q_{95} (12.6) in the data set.

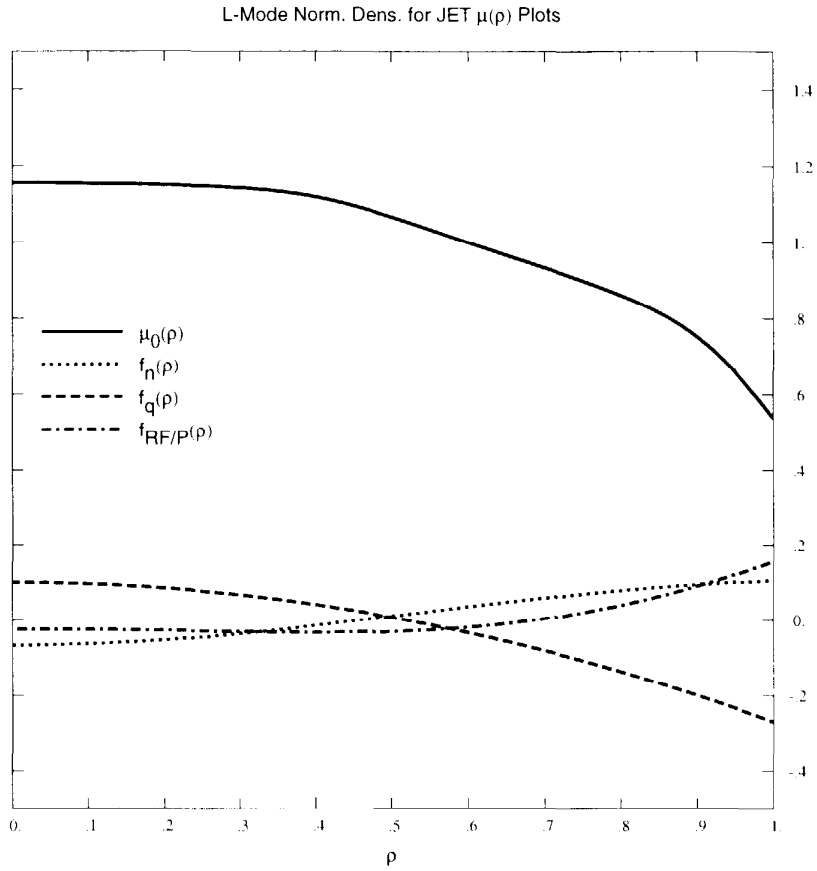


Figure 5

FIG.5. Fit functions for the normalised L-mode density profiles. The canonical profile, $\mu(\rho)$, is the predicted profile at $\bar{n} = 2.09 \cdot 10^{19} \text{ m}^{-3}$, $q_{95} = 5.066$, and $H_T = .471$. Increasing \bar{n} results in hollow profiles.

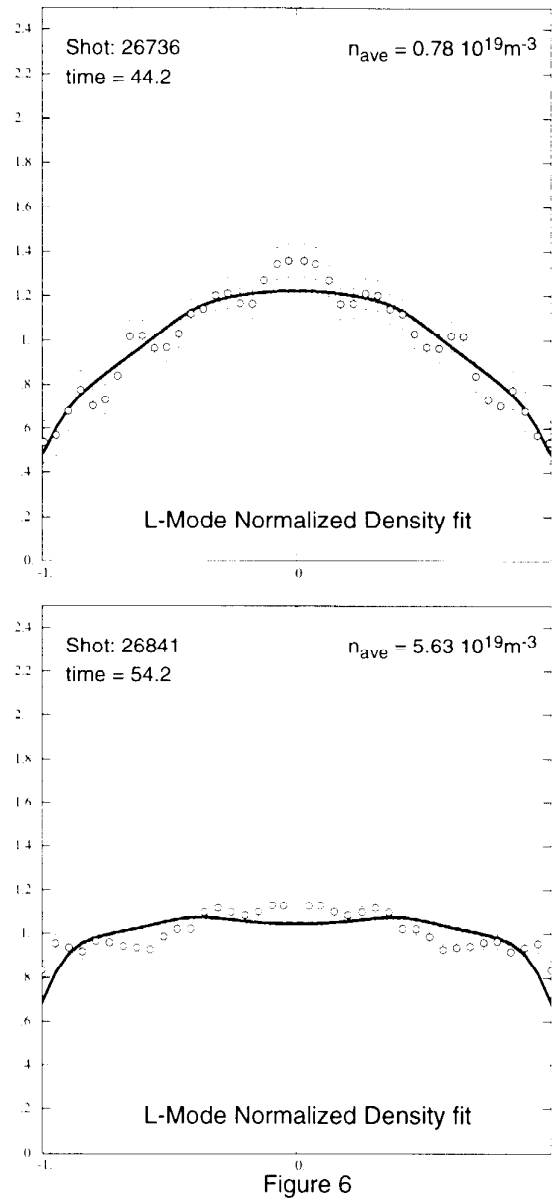


FIG.6. Normalised data versus the predicted L-mode density profile. The broader curve (JET discharge #26841 at time = 54.2 sec) has the largest value of $\bar{n} = 5.63 \cdot 10^{19} m^{-3}$ in the data set. The narrower curve (JET discharge #26736 at time = 44.2 sec) has the smallest value of $\bar{n} = 0.78 \cdot 10^{19} m^{-3}$ in the data set.

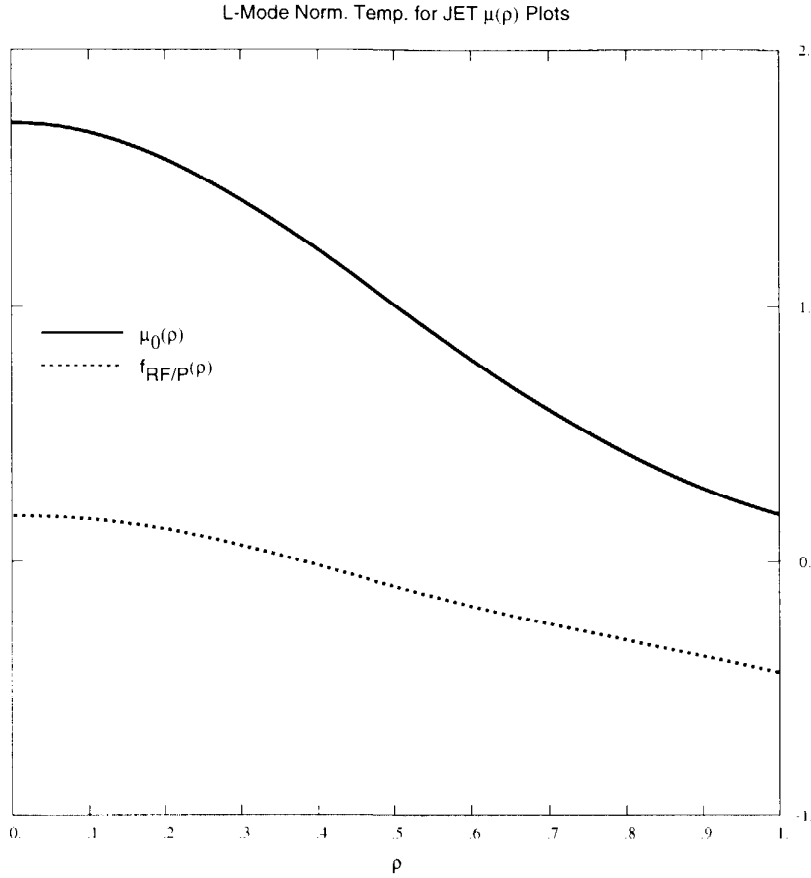


Figure 7

FIG. 7. Fit functions for the L-mode temperature. The canonical profile, $\mu(\rho)$, has a Gaussian shape with the temperature gradient decreasing outside of $\rho = 0.8$. Only the heating type fraction is important in determining the profile shape. As the percentage of ICRH power increases, the profiles become more peaked, as seen from the inferred $H f_H(\rho)$ curve. Here $\mu(\rho)$ corresponds to the predicted profile when the heating fraction is .471, corresponding to the database mean.

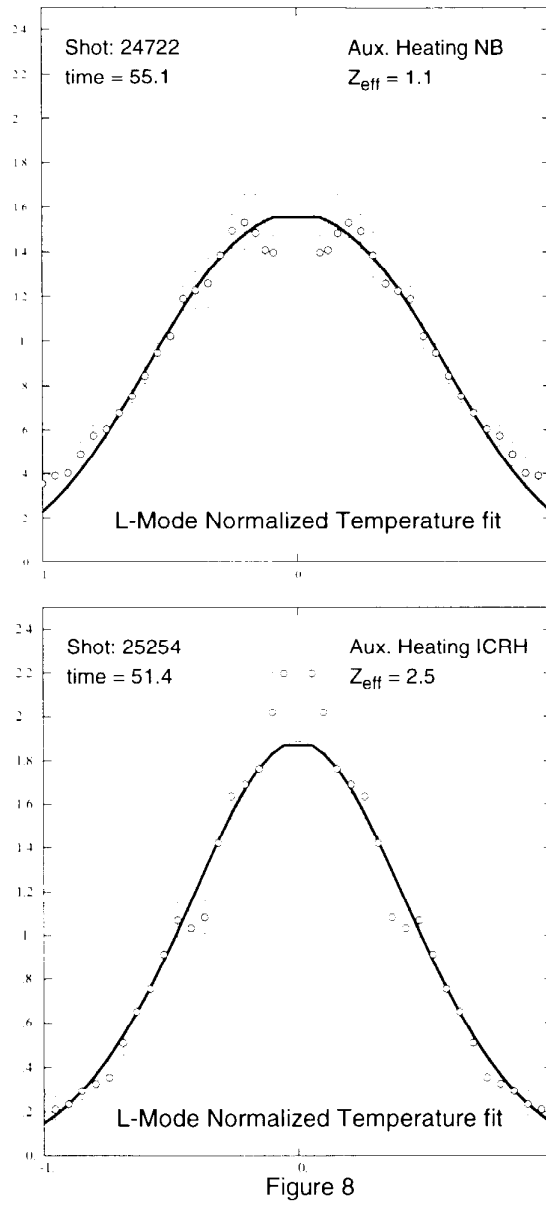


Figure 8

FIG. 8. Normalised data versus the predicted L-mode temperature profile. The broader curve (JET discharge #24722 at time = 55.1 sec) has the smallest value of Z_{eff} (1.1) for a NBI discharge (in the data set). The narrower curve (JET discharge #25254 at time = 51.4 sec) has the largest Z_{eff} (2.5) of the ICRH discharges in the data set.

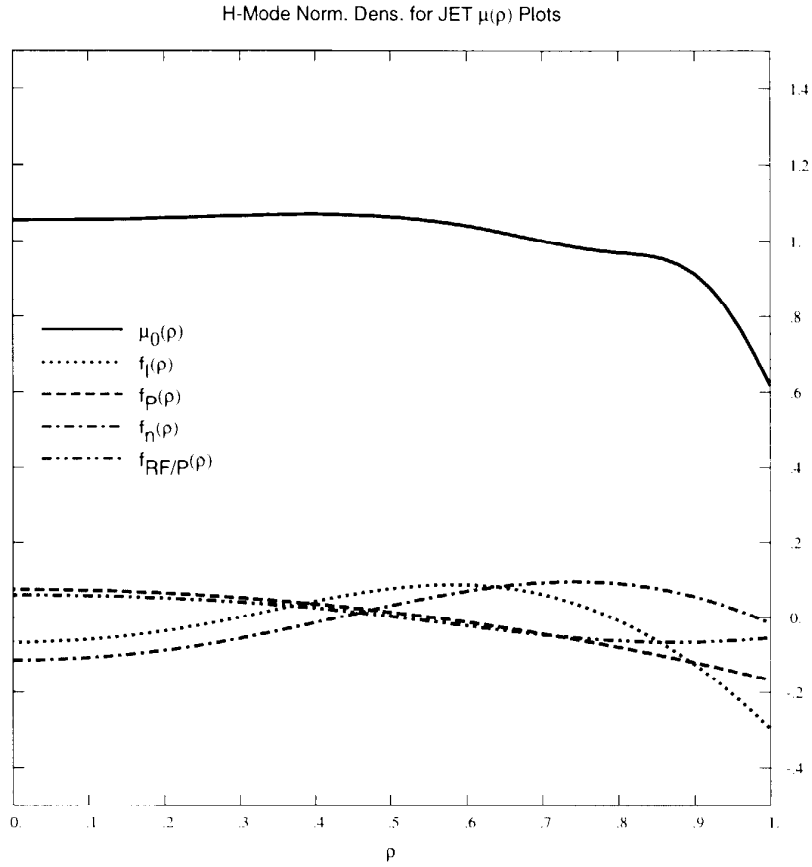


Figure 9

FIG. 9. Fit functions for the normalised H-mode density profiles. The canonical density profile is nearly flat. Here $\mu_0(\rho)$ is our predicted profile at $I_p = 2.66$ MA, $\bar{n} = 3.70 \cdot 10^{19} \text{ m}^{-3}$, $P_L = 6.32$ MW and the heating fraction, $H_{\nu} = .368$. Increasing the plasma current broadens the profile and steepens the gradient at the edge.

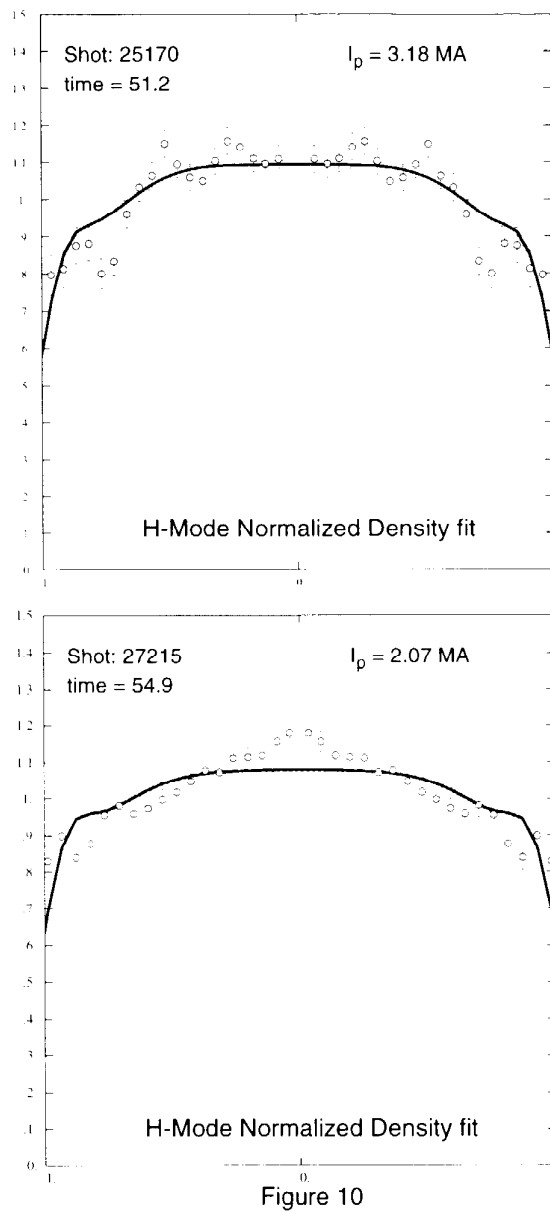


FIG. 10. Normalised data versus the predicted H-mode density profile. The broader curve (JET discharge #25170 at time = 51.2 sec) has the largest value of I_p (3.18 MA) in the data set. The narrower curve (JET discharge #27215 at time = 54.9 sec) has the smallest value of I_p (2.07) in the data set. Large values of I_p result in hollow profiles with sharp drops near the plasma edge.

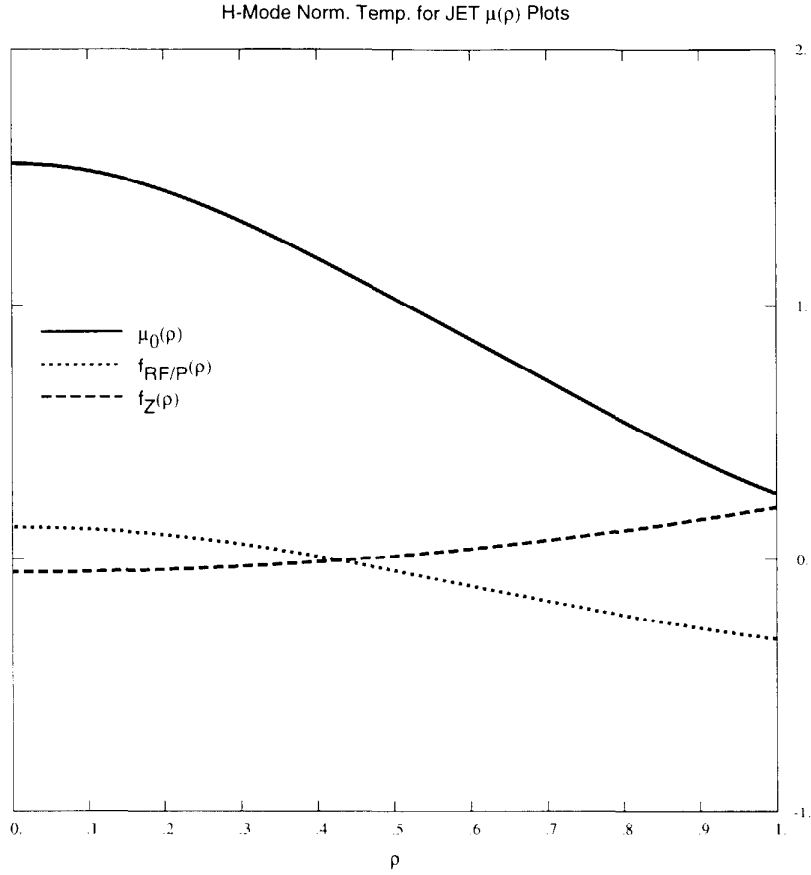


Figure 11

FIG. 11. Fit functions for the H-mode temperature. The canonical profile $\mu_0(\rho)$, is broader than the L-mode profile. Here $\mu_0(\rho)$ is our predicted profile at a heating fraction, $H_{fr} = .368$ and $Z_{eff} = 2.328$. Although the heating fraction is the most important control variable, $f_H(\rho)$ is less peaked than the corresponding function for L-mode. Since $f_{RF/P}(\rho) \approx -f_H(\rho)$, the profile shape depends only on $H_{fr} - \ln[Z_{eff}]$.

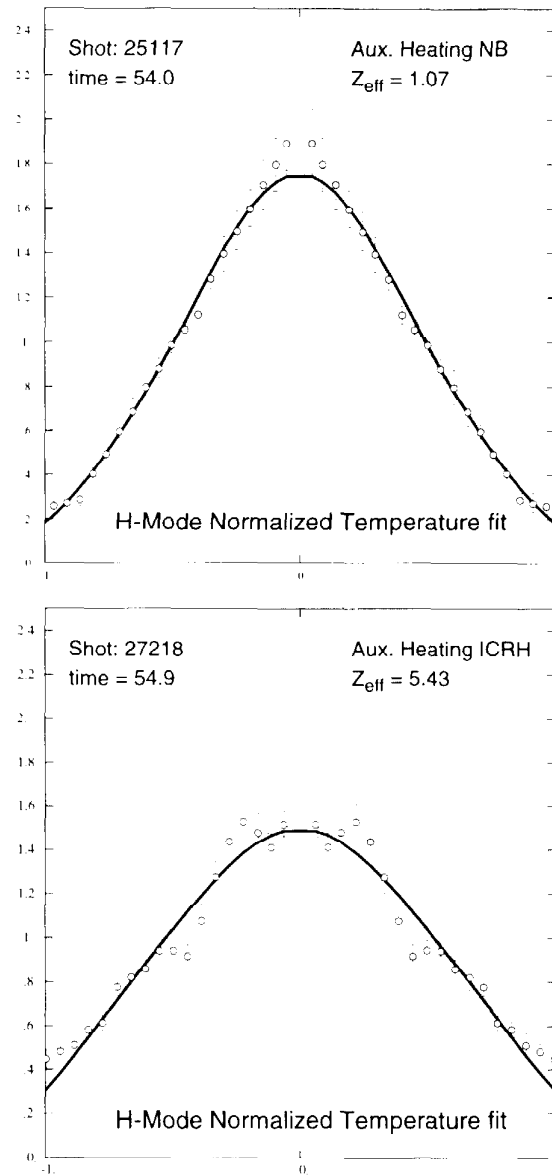


Figure 12

FIG. 12. Normalised data versus the predicted H-mode temperature profile. The narrower curve (JET discharge #25117 at time = 54.0 sec) has the largest value of Z_{eff} (1.07) for a NBI discharge in the data set. The broader curve (JET discharge #27218 at time = 54.9 sec) has the largest Z_{eff} (5.43) of the ICRH discharges in the data set. The key variable, $H_{\text{jr}} - \ln[Z_{\text{eff}}]$, is .692 for the ICRH discharge and -.068 for the NBI discharge.

Var	mean	min	max	std dev
\bar{n}	2.20	1.27	3.69	0.74
q_{95}	5.48	2.88	12.6	2.86
I_p	2.80	0.97	5.25	1.13
B_t	2.76	1.30	3.22	0.46
κ	1.44	1.30	1.75	0.122
a	1.16	1.05	1.19	0.040
R	2.92	2.83	3.01	0.047
Z_{eff}	2.10	1.20	3.35	0.60
Volt	-.35	-1.12	.914	0.66

Table 1: Ohmic database summary: Average, minimum, maximum and standard deviation of each of the control variables.

TABLES

Var	mean	min	max	std dev
\bar{n}	2.31	0.78	5.63	1.04
q_{95}	5.35	3.38	16.58	2.34
I_p	3.07	1.04	4.87	0.83
B_t	2.62	1.44	2.89	0.44
P_L	4.81	0.46	14.55	2.73
κ	1.67	1.50	1.83	0.10
Z_{eff}	-	1.07	7.61	-

Table 2: L-mode database summary: Average, minimum, maximum and standard deviation of each of the engineering control variables.

Var	mean	min	max	std dev
\bar{n}	3.85	1.878	6.73	1.19
q_{95}	5.19	3.10	6.99	1.21
I_p	2.70	2.07	3.18	0.45
B_t	2.53	1.43	2.90	0.41
P_L	8.00	0.81	12.81	2.90
κ	1.73	1.59	1.84	0.061
a	1.04	0.98	1.13	0.038
R	2.89	2.77	2.97	0.043
V_{loop}	-0.16	-1.12	0.17	0.22
Z_{eff}	2.63	1.07	7.61	1.27

Table 3: H-mode database summary: Average, minimum, maximum and standard deviation of each of the engineering variables.

Ohmic Density Goodness of Fit Table

	1 spline	2 spline	3 spline	1 spline
	PAR	PAR	PAR	PAR
\bar{n}	<u>.0612</u>	spline	spline	.0565
q_{95}	.0633	.0593	.0566	.0561
I_p	.0668	.0613	.0564	.0560
B_t	.0681	<u>.0567</u>	spline	.0567
κ	.0687	.0611	.0568	.0562
Z_{eff}	.0674	.0604	.0561	.0556
\bar{T}	.0683	.0597	.0563	.0555
\bar{n}/B	<u>.0561</u>	—	—	<u>spline</u>

Table 4: Goodness of fit of different log-additive models for the normalised Ohmic density. The “Murakami” parameter, \bar{n}/B_t , reduces the PAR statistic the most. In the third column, we compare two variable models using \bar{n} in each case. The best two variable model in column 3 is \bar{n} and B_t . The fourth column shows that adding a third control variable doesn’t improve the fit significantly. In the final column, we compare two variable models using \bar{n}/B_t in each case. Using only the ratio of \bar{n}/B_t outperforms using both \bar{n} and B_t separately because fewer degrees of freedom are used in the fit.

Normalised Ohmic Temperature Goodness of Fit Table

	1 spline	2 spline	3 spline
	PAR	PAR	PAR
\bar{n}	.0969	.0818	.0776
q_{95}	<u>.0812</u>	spline	spline
I_p	.0863	.0779	.0748
V_{loop}	.0995	.0818	.0763
B_t	.0933	<u>.0755</u>	spline
κ	.0963	.0790	.0737
Z_{eff}	.0888	.0789	.0760
\bar{T}	.0961	.0804	.0761

Table 5: Goodness of fit of different log-additive models for the normalised Ohmic temperature. The last row shows that the profile shape does not depend on the line average temperature, \bar{T} , thereby justifying our normalisation. The edge safety factor, q_{95} , reduces the PAR statistic the most. In the second column, we compare two variable models using q_{95} in each case. The best two variable model is q_{95} and B_t . The final column shows that adding a third control variable doesn't improve the fit significantly. Since κ varies little, the κ dependence is probably due to hidden variables associated with machine operation.

L-mode Density Goodness of Fit Table

Contr	1 spline	2 spline	3 spline	4 spline
2-5 Var.	PAR	PAR	PAR	PAR
q_{95}	.0667	<u>.0619</u>	spline	spline
\bar{n}	<u>.0633</u>	spline	spline	spline
I_p	.0714	.0634	.0623	.0610
B_t	.0705	.0637	.0621	.0609
κ	.0668	.0627	.0607	.0605
\bar{n}/B_t	.0641	.0635	.0619	.0609
P_L	.0714	.0626	.0613	.0603
H_{fr}	.0688	.0628	<u>.0606</u>	spline
Z_{eff}	.0672	.0639	.0623	–
\bar{T}	.0706	.0632	.0610	.0606

Table 6: Goodness of fit of different log-additive models for the normalised L-mode density. “Spline” variables are included in each run in that column. We then add the variable that reduces the criterion the most. The line average density improves the fit the most, followed by adding the edge q and then the heating fraction. Adding a fourth control variable only slightly improves the goodness of fit.

Temperature L-mode Goodness of Fit Table

Contr	1 spline	2 spline	3 spline	4 spline
Var	PAR	PAR	PAR	PAR
q_{95}	.1034	.0873	.0871	.0872
\bar{n}	.1025	<u>.0868</u>	spline	spline
I_p	.1020	.0875	.0874	.0874
B_t	.1012	.0874	.0872	.0873
\bar{n}/B_t	.1035	.0869	.0872	.0875
κ	.0960	.0874	.0866	.0865
P_L	.1033	.0873	<u>.0868</u>	spline
H_{fr}	<u>.0869</u>	spline	spline	spline
Z_{eff}	.102	.0868	.0871	–
\bar{T}	.102	.0873	.0870	.0873

Table 7: Goodness of fit of different log-additive models for the L-mode temperature. The L-mode temperature depends almost exclusively on the type of heating. Adding more traditional control variables does not improve the fit. Even using four control variables gives a fit roughly comparable to the fit using only the heating fraction. The last row shows that the profile shape does not depend on the line average temperature, \bar{T} . Thus the size and shape of the temperature have little correlation.

H-mode Density Goodness of Fit Table

Contr	1 spline	2 splines	3 splines	4 splines
Var	PAR	PAR	PAR	PAR
\bar{n}	.0645	.0617	<u>.0584</u>	<u>.0563</u>
q_{95}	.0625	.0614	.0596	.0585
I_p	<u>.0619</u>	spline	spline	spline
B_t	.0650	.0613	.0597	.0587
Z_{eff}	.0647	.0612	.0599	.0584
P_L	.0633	<u>.0597</u>	spline	spline
H_{fr}	.0638	.0603	<u>.0583</u>	spline

Table 8: Goodness of fit of different log-additive models for the normalised H-mode density. The plasma current is the most important control variable followed by the loss power. At the third stage, both \bar{n} and the heating fraction are equally effective in reducing the PAR statistic. This table illustrates a difficulty of sequential variable selection: Occasionally, there is no clear cutoff in the number or choice of terms to include. We select the four-variable model because the PAR value continues to decrease and the $(I_p, P_L, \bar{n}, H_{fr})$ model is clearly superior to other four variable models.

H-mode Temperature Goodness of Fit Table

Contr	1 spline	2 spline	3 spline	4 spline
Var.	PAR	PAR	PAR	PAR
\bar{n}	.0738	.0640	.0630	spline
q_{95}	.0735	.0655	.0639	.0634
I_p	.0739	.0645	.0641	.0636
B_t	.0700	.0646	.0638	.0632
κ	.0697	.0652	.0636	.0633
Z_{eff}	.0728	<u>.0632</u>	spline	spline
P_L	.0738	.0648	.0636	.0625
H_{fr}	<u>.0650</u>	spline	spline	spline
\bar{T}	.0726	.0562	.0640	.0634

Table 9: Goodness of fit of different log-additive models for the ELM-free H-mode temperature. The most important control variable is the the heating fraction of ICRH power. Adding Z_{eff} to the model results in a significant improvement in fit. No significant reduction in the PAR statistic occurs when a third control variable is added.

Scaling Expressions for Profiles

	Ohmic	L-Mode	H-Mode
density	$\tilde{n}(\rho) = \mu(\rho) \left(\frac{\bar{n}}{B_t}\right)^{f_{n/B}(\rho)}$	$\tilde{n}(\rho) = \mu(\rho) (\bar{n})^{f_n(\rho)} q_{95}^{f_q(\rho)}$	$\tilde{n}(\rho) = \mu(\rho) I_p^{f_I(\rho)} P_L^{f_P(\rho)} (\bar{n})^{f_n(\rho)}$
shape		$\times \exp[f_H(\rho) H_{fr}]$	$\times \exp[f_H(\rho) H_{fr}]$
temperature	$\tilde{T}(\rho) = \mu(\rho) q_{95}^{f_q(\rho)} B_t^{f_B(\rho)}$	$\tilde{T}(\rho) = \mu(\rho) \times$	$\tilde{T}(\rho) = \mu(\rho) \times$
shape		$\exp[f_H(\rho) H_{fr}]$	$\exp[f_H(\rho) H_{fr}] Z_{eff}^{f_Z(\rho)}$
Line average	$\bar{T} \sim I_p^{.64} B_t^{.54} (\bar{n})^{-.31}$	$\bar{T} \sim B_t^{.97} P_L^{.36} (\bar{n})^{-.38}$	$\bar{T} \sim I_p^{1.22} P_L^{.29} (\bar{n})^{-.253}$
temperature			$\exp[.24 H_{fr}]$

Table 10: Summary of scaling dependencies for profiles. The normalised profiles are denoted by $\tilde{n}(\rho) \equiv n(\rho)/\bar{n}$ and $\tilde{T}(\rho) \equiv T(\rho)/\bar{T}$.